



# Infrared Energy Harvesting in Millimeter-Scale GaAs Photovoltaics

Eunseong Moon, *Student Member, IEEE*, David Blaauw, *Fellow, IEEE*,  
and Jamie D. Phillips, *Senior Member, IEEE*

**Abstract**—The design and characterization of millimeter-scale GaAs photovoltaic (PV) cells are presented and demonstrate highly efficient energy harvesting in the near infrared (NIR). Device performance is improved dramatically by optimizing the device structure for the NIR spectral region and improving surface and sidewall passivation with the ammonium sulfide treatment and subsequent silicon nitride deposition. The power conversion efficiency of a 6.4-mm<sup>2</sup> cell under 660-nW/mm<sup>2</sup> NIR illumination at 850 nm is greater than 30%, which is higher than commercial crystalline silicon solar cells under similar illumination conditions. Critical performance limiting factors of submillimeter-scale GaAs PV cells are addressed and compared to theoretical calculations.

**Index Terms**—Gallium arsenide, photovoltaics (PVs), silicon, wireless energy harvesting.

## I. INTRODUCTION

WIRELESS energy harvesting for biomedical implantable devices is an attractive technology for a wide range of biomedical applications for measuring physiological signals [1]–[5]. Fully implanted systems [4], [5] were developed recently with the aid of wireless energy harvesting methods [6]–[9] utilizing kinetic energy, ultrasonic mechanical vibrations for piezoelectric energy harvesting, thermal energy, and radio frequency (RF) electromagnetic radiation for inductive coupling link. The main hurdles [7], [8], [10] for these wireless energy harvesting are the robustness of ambient energy sources through the biological tissue or skull and miniaturization of implantable devices. Photovoltaic (PV) energy harvesting provides an alternative means of wireless power transfer (WPT) through the near-infrared (NIR) optical transparency window of the biological tissue between 650- and 950-nm range [11], [12],

Manuscript received July 6, 2017; revised August 14, 2017; accepted August 24, 2017. Date of publication September 6, 2017; date of current version October 20, 2017. This work was supported in part by the National Science Foundation and in part by the National Institutes of Health under Award R01CA195655. The content is solely the responsibility of the authors and does not necessarily represent the official views of the National Science Foundation or National Institutes of Health. The review of this paper was arranged by Editor A. G. Aberle. (*Corresponding author: Eunseong Moon.*)

The authors are with the Department of Electrical Engineering and Computer Science, University of Michigan, Ann Arbor, MI 48109 USA (e-mail: esmoon@umich.edu; blaauw@umich.edu; jphilli@umich.edu).

Color versions of one or more of the figures in this paper are available online at <http://ieeexplore.ieee.org>.

Digital Object Identifier 10.1109/TED.2017.2746094

where the ambient solar irradiation or an intentional light-emitting diode (LED) illumination could provide energy to implantable PV cells and conventional high-efficiency PV cells [13] convert this NIR wavelength region efficiently with above 90% external quantum efficiency (EQE). The key challenges to obtaining highly efficient PV energy harvesting are that device performances of PV cells at millimeter scale or smaller under low-flux illumination are degraded by the shunt resistance [14]–[16] and sidewall/perimeter recombination losses [14], [17], [18]. Previous works on NIR PV WPT [19]–[22] are centimeter scale or larger and tested under extremely high intensity of laser illumination in milliwatt range producing skin heating [7], [22]. One of the previously reported silicon PV cells at millimeter scale [17], [23] addressed and relatively overcame these challenges, which had above 17% power conversion efficiency under low-flux NIR illumination below 1  $\mu$ W/mm<sup>2</sup> at a wavelength of 850 nm. However, fundamental material characteristics of silicon such as higher dark current and shunt leakage compared to other III–V compound semiconductors limit the open-circuit voltage and corresponding power conversion efficiency. On the other hand, GaAs-based PV cells have a possibility to boost the NIR energy harvesting efficiency due to superior optical properties matched to desired NIR wavelength region, low dark current and low shunt leakage, which worked successfully under low-flux indoor conditions [14], [15]. The feasibility of subcutaneous energy harvesting utilizing fabricated silicon and GaAs PV cells through the NIR transparency window, and possible encapsulation methods for these PV cells were discussed and evaluated in previous papers [17], [23] and could provide sufficient power for millimeter-scale systems. In this paper, the details of submillimeter-scale GaAs PVs cells optimized for low-flux NIR energy harvesting at a wavelength of 850 nm and their performance limiting factors are explored.

## II. EXPERIMENT

The material layer structure of GaAs PV cell for NIR energy harvesting was optimized based on simulation results using Synopsys Sentaurus Device [24] using widely accepted material parameters at 300 K and neglecting recombination effects from the surface/sidewall. The device structure grown by molecular beam epitaxy utilizing the structure of conventional high-efficiency GaAs solar cells [25] consists of n-base and

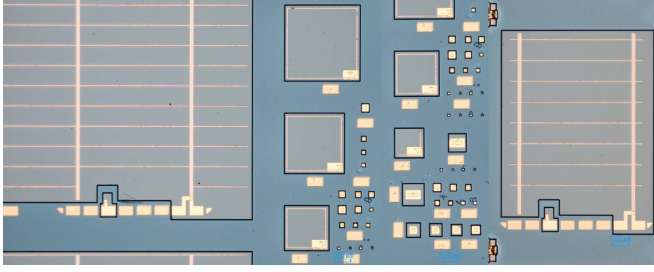


Fig. 1. Fabricated variable size of PV cells from 0.001 to 6.4 mm<sup>2</sup>.

TABLE I  
OPTIMIZED DEVICE STRUCTURE UNDER ILLUMINATION  
OF 100 nW/mm<sup>2</sup> AT 850 nm

Type	Material	Thickness (nm)	Doping (cm <sup>-3</sup> )
p++	GaAs	200	2 x 10 <sup>19</sup>
p+	Al <sub>0.8</sub> Ga <sub>0.2</sub> As	30	2 x 10 <sup>18</sup>
p+	GaAs	500	4 x 10 <sup>18</sup>
n-	GaAs	50	1 x 10 <sup>16</sup>
n-	GaAs	200	Graded
n	GaAs	2750	1 x 10 <sup>17</sup>
n+	Al <sub>0.3</sub> Ga <sub>0.7</sub> As	150	1 x 10 <sup>18</sup>
n+	GaAs	300	2 x 10 <sup>18</sup>

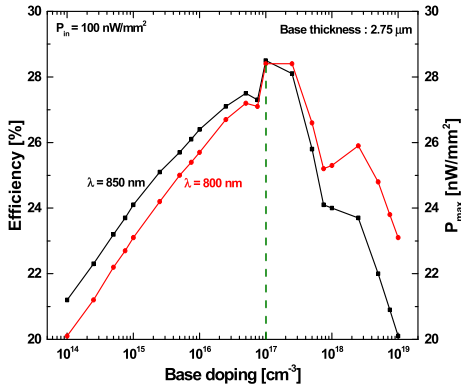


Fig. 2. Simulated maximum power density under 100-nW/mm<sup>2</sup> illumination at 800 and 850 nm versus variable base doping concentration.

p-emitter layers with the addition of p-Al<sub>0.8</sub>Ga<sub>0.2</sub>As window and n-Al<sub>0.3</sub>Ga<sub>0.7</sub>As back surface field layers on a heavily doped GaAs substrate, as shown in Table I. The device parameters are designed for a center wavelength at the first optical transparency window (650–950 nm) [11], [12] through the biological tissue between 800 and 850 nm, under low-intensity illumination at 100 nW/mm<sup>2</sup>. The power conversion efficiency is strongly dependent on the doping concentration (Fig. 2) and thickness of the base layer. The base doping concentration of 10<sup>17</sup>cm<sup>-3</sup> and the base thickness of 2.75- $\mu$ m result in the maximum output-power density under 100 nW/mm<sup>2</sup> at a wavelength range between 800 and 850 nm. The optimized device parameters are summarized in Table I. Devices with varying area were fabricated (Fig. 1) to study the influence of sidewall/perimeter recombination losses [14], [17], [18], ranging

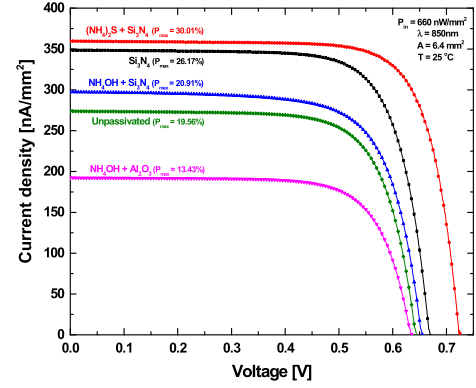


Fig. 3. Measured current density versus voltage curves of different passivation studies of 6.4-mm<sup>2</sup> cell under 850-nm NIR-LED illumination with 660 nW/mm<sup>2</sup>.

from 0.001 to 6.4 mm<sup>2</sup>, corresponding to perimeter/area ( $P/A$ ) ratio from 125 to 1.69 mm<sup>-1</sup>. Various passivation processes were studied including the dielectric passivation and chemical passivation methods to reduce the sidewall/perimeter recombination losses, including plasma enhanced chemical vapor deposition (PECVD) Si<sub>3</sub>N<sub>4</sub>, (NH<sub>4</sub>)<sub>2</sub>S [26]–[28], NH<sub>4</sub>OH with subsequent PECVD Si<sub>3</sub>N<sub>4</sub>, and NH<sub>4</sub>OH with subsequent atomic layer deposition (ALD) Al<sub>2</sub>O<sub>3</sub> [29]. Further details of the different passivation processes are as follows: 1) 100-nm PECVD Si<sub>3</sub>N<sub>4</sub> at 380 °C; 2) (NH<sub>4</sub>)<sub>2</sub>S (23% in H<sub>2</sub>O) for 10 min at room temperature + 100-nm PECVD Si<sub>3</sub>N<sub>4</sub> at 380 °C; 3) NH<sub>4</sub>OH (29% in H<sub>2</sub>O) for 3 min at room temperature + 100-nm PECVD Si<sub>3</sub>N<sub>4</sub> at 380 °C; 4) NH<sub>4</sub>OH (29% in H<sub>2</sub>O) for 3 min at room temperature + 25-nm ALD Al<sub>2</sub>O<sub>3</sub> at 150 °C; and 5) a sample without passivation.

Current–voltage ( $J$ – $V$ ) and power–voltage ( $P$ – $V$ ) characteristics of fabricated cells under dark and illumination conditions were measured using Keithley 2400 and 4200 semiconductor characterization tools. A microscope-compatible NIR-LED with 850-nm center wavelength and a calibrated power-meter were used to control low-flux illumination in increments of 5 nW/mm<sup>2</sup>. Passivation effects on device performances of variable size cells were tested under 660 nW/mm<sup>2</sup> illumination at 850 nm, which is realistic under subcutaneous conditions and much lower flux than AM 1.5 sunlight at 1000- $\mu$ W/mm<sup>2</sup> illumination [30]. The EQE was measured using a calibrated photodetector, lock-in amplifier, monochromator, optical chopper, and xenon white light source.

### III. RESULTS

#### A. Passivation Layer

The  $J$ – $V$  characteristics of 6.4-mm<sup>2</sup> GaAs PV cells passivated with the five different passivation layers under 660-nW/mm<sup>2</sup> illumination at a wavelength of 850 nm are shown in Fig. 3. A 100-nm PECVD Si<sub>3</sub>N<sub>4</sub> passivation layer matched to the NIR tissue transparency window as shown in Fig. 4 increased the short-circuit current ( $J_{SC}$ ) compared to control sample without passivation by reducing the surface reflectance and the surface recombination loss. The ammonium sulfide ((NH<sub>4</sub>)<sub>2</sub>S) treatment encapsulated with the PECVD

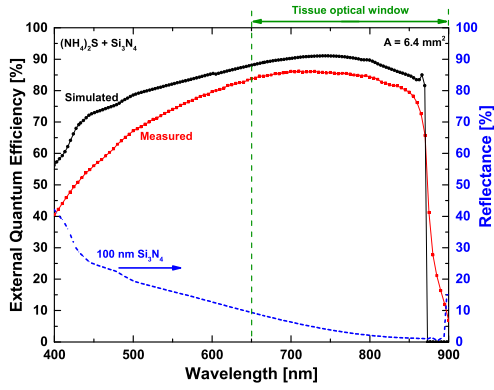


Fig. 4. Measured and Simulated (dashed) EQE characteristics of  $(\text{NH}_4)_2\text{S} + \text{Si}_3\text{N}_4$  passivated sample along with the wavelength range between 400 and 900 nm.

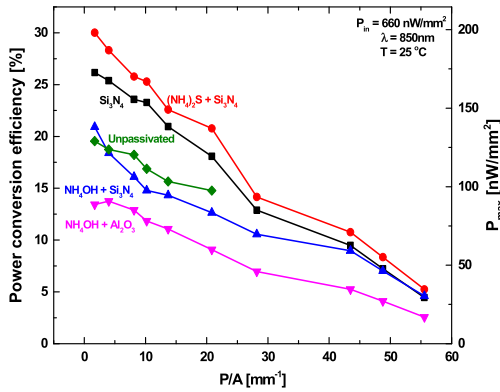


Fig. 5. Measured power conversion efficiency values of various passivation studies versus  $P/A$  ( $\text{mm}^{-1}$ ) ratio from 1.69 to  $55.56 \text{ mm}^{-1}$  corresponding device size from 6.4 to  $0.0052 \text{ mm}^2$ .

$\text{Si}_3\text{N}_4$  layer for long-term stability of passivation layers [31] improved both the short-circuit current density ( $J_{\text{SC}}$ ) and the open-circuit voltage ( $V_{\text{OC}}$ ), which results in the maximum power conversion efficiency above 30% under 850-nm NIR illumination with  $660 \text{ nW/mm}^2$  and can supply sufficient power to a millimeter-scale system with the minimum power requirement of  $50 \text{ nW/mm}^2$  [32].

The EQE measurement as shown in Fig. 4 on this  $(\text{NH}_4)_2\text{S}$  passivated sample shows that the device structure is well optimized for the first optical window in the NIR wavelength range with above 80% EQE and 5%–7% discrepancy between simulated and measured EQE values is observed over the desired wavelength region due to the surface reflection from metal fingers. Further studies of different passivation layer effects on device performance for variable size of cells from  $0.0052$  to  $6.4 \text{ mm}^2$  corresponding  $P/A$  ratio  $55.56$  to  $1.69 \text{ mm}^{-1}$  are shown in Fig. 5. The device performance of cells with varying size cells is strongly dependent on the  $P/A$  ratio, illustrating the critical impact of sidewall recombination loss as one of the most critical limiting factors for these small-area PV cells [14], [17], [18], as discussed further in Section IV. The  $(\text{NH}_4)_2\text{S}$  treatment improved  $V_{\text{OC}}$  values of various size PV cells and this  $V_{\text{OC}}$  improvement is closely relevant to the reduction in the reverse saturation

TABLE II  
EXTRACTED PARAMETERS OF  $6.4\text{-mm}^2$  CELLS USING (1)

Passivation	$J_0$ (PA/MM <sup>2</sup> )	n
$\text{Si}_3\text{N}_4$	0.6157	1.939
$(\text{NH}_4)_2\text{S} + \text{Si}_3\text{N}_4$	0.0673	1.801
$\text{NH}_4\text{OH} + \text{Si}_3\text{N}_4$	0.5853	1.933
$\text{NH}_4\text{OH} + \text{Al}_2\text{O}_3$	0.4532	1.906
Unpassivated	0.9038	1.969

current ( $J_0$ ) as indicated in (1)

$$V_{\text{OC}} = \frac{nkT}{q} \ln \left( \frac{J_{\text{SC}}}{J_0} + 1 \right) \quad (1)$$

where  $n$  is the ideality factor,  $k$  is Boltzmann's constant,  $T$  is the temperature,  $J_0$  is the reverse saturation current density, and  $J_{\text{SC}}$  is the short-circuit current density. The  $(\text{NH}_4)_2\text{S}$  treatment [26]–[28] etched the native oxide on the surface/sidewall and effectively passivated the dangling bonds with additional sulfur bonds, resulting in the reduction of  $J_0$ . The  $\text{NH}_4\text{OH}$  treatment reduced  $J_{\text{SC}}$  due to increased optical scattering from the rough surface though the  $\text{NH}_4\text{OH}$  treatment etched the native oxide [29] to achieve more electronically favorable surface properties before the dielectric passivation. The 25-nm ALD  $\text{Al}_2\text{O}_3$  did not provide an optimal antireflection match to the desired wavelength at 850 nm, which increased the surface reflectance over the desired wavelength region more than the optimized 100-nm PECVD  $\text{Si}_3\text{N}_4$  layer, resulting in a reduction in  $J_{\text{SC}}$ . The detailed device parameters regarding p-n junction diode equations and recombination losses were extracted from results of dark current measurement.

## B. Dark Current Measurements

Dark current measurements were conducted on all PV cells with varying  $P/A$  ratio to examine the impact of surface passivation properties. The dark  $J$ - $V$  plots of  $0.25\text{-mm}^2$  samples are shown in Fig. 6(a) and the extracted  $J_0$  parameters are shown in Fig. 6(b) obtained by curve fitting to the forward bias region between 0 and 0.7 V using the one-diode equation

$$J = J_0 \left[ \exp \left( \frac{qV}{nkT} \right) - 1 \right] \quad (2)$$

where  $J$  is the total current density,  $J_0$  is the reverse saturation current,  $V$  is the applied voltage,  $k$  is Boltzmann's constant, and  $T$  is the temperature. The extracted  $J_0$  parameters for all passivation studies shown in Fig. 6(b) show the clear  $P/A$  ratio dependence due to increased sidewall/perimeter recombination losses as expected. The dramatic reduction in  $J_0$  over all measured PV cells from  $(\text{NH}_4)_2\text{S}$  treatment was also observed in Fig. 6(b). For example, extracted  $J_0$  of  $6.4\text{-mm}^2$  PV cells summarized in Table II was reduced from  $0.9038 \text{ pA/mm}^2$  for the sample without passivation to  $0.0673 \text{ pA/mm}^2$  for the sample passivated with  $(\text{NH}_4)_2\text{S} + \text{PECVD Si}_3\text{N}_4$ , agreeing with the improvement in  $V_{\text{OC}}$  as indicated in Fig. 5.

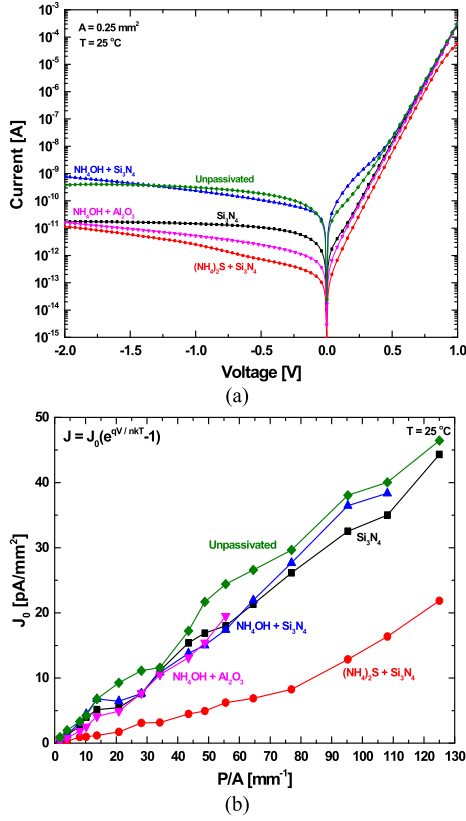


Fig. 6. (a) Measured current versus voltage of 0.25-mm<sup>2</sup> sample under dark conditions. (b) Extracted reverse saturation current values of different passivation studies versus  $P/A$  (mm<sup>-1</sup>) ratio from 1.69 to 125 mm<sup>-1</sup> corresponding device size from 6.4 to 0.001 mm<sup>2</sup>.

The diode ideality factor ( $n$ ) of 6.4-mm<sup>2</sup> cells summarized in Table II supported previous results that the ideality factor values near  $n = 2$  for samples are dominated by the space charge region (SCR) recombination losses [14] mainly connected to the sidewall recombination losses and the (NH<sub>4</sub>)<sub>2</sub>S treatment with subsequent Si<sub>3</sub>N<sub>4</sub> deposition reduced the diode ideality factor from 1.969 to 1.801, suggesting that the sulfur treatment unpinned the Fermi-level [31] and reduced the SCR recombination losses from surface and sidewall regions [33], [34]. Numerical parameters relevant to the perimeter recombination losses can be extracted by curve fitting to the forward bias region using the two-diode equation

$$J = J_{01} \left[ \exp\left(\frac{qV}{kT}\right) - 1 \right] + J_{02} \left[ \exp\left(\frac{qV}{2kT}\right) - 1 \right] \quad (3)$$

where  $J_{01}$  and  $J_{02}$  are the saturation current densities for carrier recombination in the quasi-neutral region and in the SCR, respectively. The extracted  $J_{02}$  along with  $P/A$  ratio are plotted in Fig. 7. The extracted  $J_{02}$  exhibiting the strong linear  $P/A$  dependence can be expanded as (4) [18], [35]

$$J_{02} = J_{02B} + J'_{02P} \left( \frac{P}{A} \right) \quad (4)$$

where  $J_{02B}$  is the bulk recombination current density and  $J'_{02P}$  (A/mm) is the perimeter recombination coefficient. These coefficients extracted using the linear curve fitting to  $J_{02}$  using (4) are summarized in Table III, which indicate that the effect of Si<sub>3</sub>N<sub>4</sub> passivation mainly

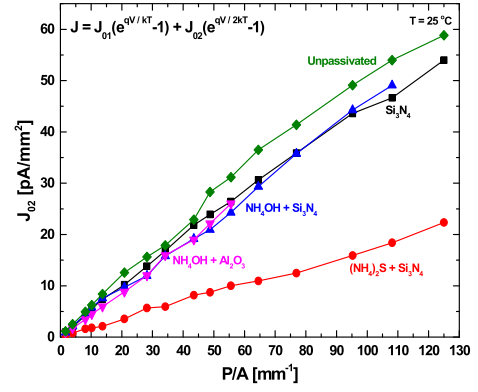


Fig. 7. Extracted  $J_{02}$  parameters along with  $P/A$  (mm<sup>-1</sup>) ratio from 1.69 to 125 mm<sup>-1</sup>.

TABLE III  
EXTRACTED PARAMETERS USING (2) AND (3)

Passivation	$J_{02B}$ (pA/MM <sup>2</sup> )	$J'_{02P}$ (pA/mm)	$S_0L_S$ (cm <sup>2</sup> /s)
Si <sub>3</sub> N <sub>4</sub>	0.7831	0.4596	13.66
(NH <sub>4</sub> ) <sub>2</sub> S + Si <sub>3</sub> N <sub>4</sub>	0.1409	0.1714	5.09
NH <sub>4</sub> OH + Si <sub>3</sub> N <sub>4</sub>	0.313	0.4507	13.4
NH <sub>4</sub> OH + Al <sub>2</sub> O <sub>3</sub>	0.0438	0.4518	13.43
Unpassivated	1.934	0.4882	14.51

reduced the bulk recombination current density from 1.934 to 0.7831 pA/mm<sup>2</sup> rather than the perimeter recombination loss from 0.4882 to 0.4596 pA/mm compared to the control sample without passivation. The additional NH<sub>4</sub>OH treatment with Si<sub>3</sub>N<sub>4</sub> passivation also had a slight improvement in the perimeter recombination loss and made the optimized passivation to the bulk recombination only. ALD Al<sub>2</sub>O<sub>3</sub> passivation reduced the bulk recombination losses significantly from 1.934 to 0.0438 pA/mm<sup>2</sup>, but had a little impact on reducing the perimeter recombination loss. However, the (NH<sub>4</sub>)<sub>2</sub>S treatment reduced both for bulk and perimeter recombination losses dramatically from 1.934 to 0.1409 pA/mm<sup>2</sup> for the bulk recombination and from 0.4882 to 0.1714 pA/mm for the perimeter recombination, suggesting that the exposed mesa edges were effectively passivated with additional sulfur bonds.

The important parameters relevant to  $J'_{02P}$  can be extracted using (5) [18], [35]

$$J'_{02P} = qn_i S_0 L_S \quad (5)$$

where  $n_i$  is the intrinsic carrier concentration,  $S_0$  is the surface recombination velocity, and  $L_S$  is the effective surface diffusion length. The extracted  $S_0L_S$  product of the (NH<sub>4</sub>)<sub>2</sub>S treated sample was 5.09 cm<sup>2</sup>/s where the high-efficiency GaAs-based solar cells had  $S_0L_S < 1$  cm<sup>2</sup>/s [18], [35], [36]. Further improvements in the device structure and passivation studies are still needed to overcome the perimeter recombination losses.

### C. Shunt Resistance

The degradation from the parasitic shunt resistance dominating the device operation under low-flux illumination [14]–[16]

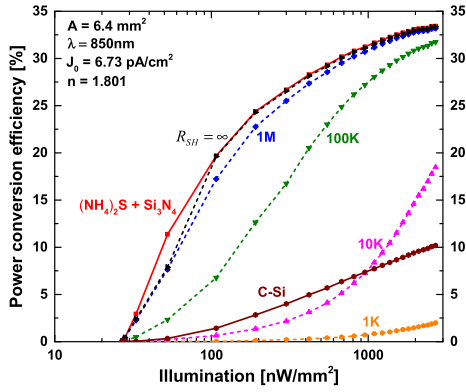


Fig. 8. Measured (solid) power conversion efficiency values under NIR illumination at a wavelength of 850 nm for the  $(\text{NH}_4)_2\text{S} + \text{Si}_3\text{N}_4$  passivated PV cell and for commercial c-Si solar cell for comparison. Simulated (dashed) values varying shunt resistance in  $(\Omega \cdot \text{cm}^2)$  are shown using extracted  $J_0$  and  $n$  diode parameters shown in the inset.

was investigated for the sample with  $(\text{NH}_4)_2\text{S} + \text{Si}_3\text{N}_4$  passivation varying the illumination intensities, as shown in Fig. 8. The simulated values for the comparison were calculated using the diode (6)

$$J = J_{sc} - J_0 \left[ \exp \left( \frac{q(V + JAR_s)}{nkT} \right) - 1 \right] - \frac{V + JAR_s}{R_{sh}} \quad (6)$$

where  $J_{sc}$  is the short-circuit current,  $R_s$  is the parasitic series resistance, and  $R_{sh}$  is the parasitic shunt resistance, using numerical extracted diode parameters from Table II and varying the shunt resistance values in  $\Omega \cdot \text{cm}^2$ . As shown in Fig. 8, the performances of measured GaAs PV cell under various NIR illumination conditions from  $30 \text{ nW/mm}^2$  to  $2.69 \mu\text{W/mm}^2$  were free of the shunt resistance degradation with above  $10\text{-M}\Omega \cdot \text{cm}^2$  shunt resistance value that is consistent with the previous GaAs PV cell results [14] though the commercial crystalline silicon solar cell [37] with above 22% power conversion efficiency under AM 1.5 solar irradiation shows the clear performance degradation from the shunt resistance under dim NIR illumination below  $1 \mu\text{W/mm}^2$ .

#### IV. DISCUSSION

The power conversion efficiency for a  $6.4\text{-mm}^2$  cell is greater than 30% under 850-nm NIR illumination at  $660 \text{ nW/mm}^2$  through the optimization of device structures and improvement in  $V_{oc}$  from optimized sidewall passivation studies using  $(\text{NH}_4)_2\text{S}$  and PECVD  $\text{Si}_3\text{N}_4$ . This efficiency approaches the expected value from simulation results neglecting surface/sidewall recombination, as shown in Fig. 10. The parasitic shunt resistance of optimized GaAs PV cell is on the order of  $10\text{-M}\Omega \cdot \text{cm}^2$  range as shown in Fig. 8, which can sufficiently overcome the shunt resistance degradation under low-flux illumination conditions. The  $J_0$  and  $J_02$  values extracted from dark  $J$ - $V$  measurements are gradually increased with increasing  $P/A$  ratio, which shows a dramatic reduction in dark current from 1.934 to  $0.1409 \text{ pA/mm}^2$  for the bulk recombination current and from 0.4882 to  $0.1714 \text{ pA/mm}$  for the perimeter recombination coefficient from the  $(\text{NH}_4)_2\text{S}$

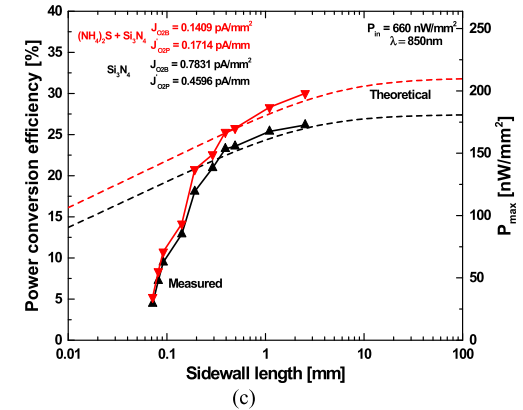
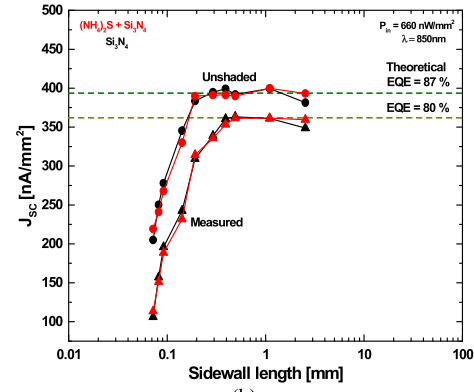
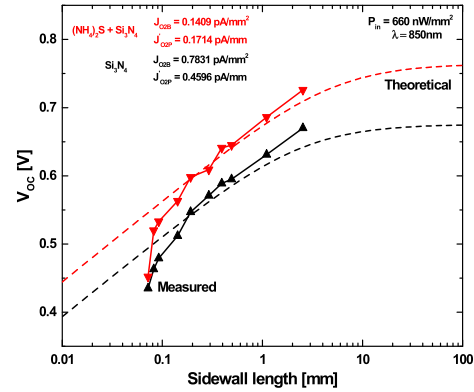


Fig. 9. Comparison with calculated (dashed) and measured (a)  $V_{oc}$  values, (b)  $J_{sc}$  values with/without the metal shadows, and (c) power conversion efficiency values for square GaAs cells with varying the sidewall length.

treatment encapsulated with PECVD  $\text{Si}_3\text{N}_4$ , attributed to the sulfur passivation of surface states [26]–[28].

The measured  $V_{oc}$  values in Fig. 9(a) agree with theoretically calculated values, showing a reduction from the increased reverse saturation current originated from the sidewall/perimeter recombination losses. The deviation of measured  $V_{oc}$  for small PV cells below  $200\text{-}\mu\text{m}$  sidewall length is relevant to  $J_{sc}$  degradation. The measured  $J_{sc}$  values as shown in Fig. 9(b) exhibit a sharp drop as cell size decreases though theoretical  $J_{sc}$  should be independent of device size. One of the major  $J_{sc}$  limiting factors for small PV cells is optical shadowing from metal fingers and pads in the light harvesting area. However, recalculated values for  $J_{sc}$  accounting

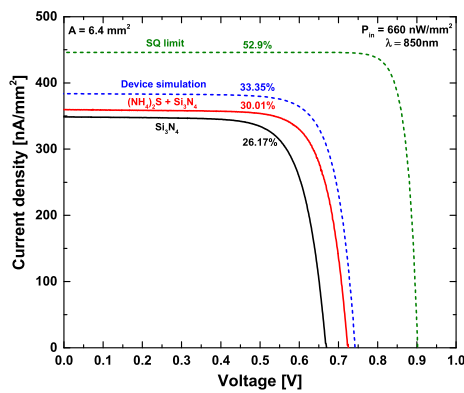


Fig. 10. Measured current density versus applied voltage characteristics with corresponding maximum power conversion efficiency and comparison to SQ model and device simulation.

for optical shadowing effects still show a similar drop below 200- $\mu\text{m}$  sidewall length. For these small micrometer-scale PV cells, a “dead area” [33] near the cell perimeter may be the cause of the substantial loss in photocurrent due to carrier diffusion to exposed sidewalls.

The overall power conversion efficiency values are shown in Fig. 9(c) and are limited by factors including an unavoidable sidewall recombination loss, optical shadowing from metal pads, and dead area near sidewall. Therefore, further improvements in power conversion efficiency approaching Shockley–Queisser (SQ) limit [38] indicated in Fig. 10 will require continued reduction in edge effects, where the surface and sidewall passivation using wide bandgap materials matched to the lattice constant of GaAs such as InGaP [39] or AlGaAs [40] may be required. The surface reflectance from metal pads might be reduced from transparent metal anode contacts such as indium tin oxide (ITO) [41], aluminum-doped zinc oxide [41], or Ti/ITO [39].

## V. CONCLUSION

GaAs PV cells at millimeter-scale and micrometer-scale were optimized for wireless energy harvesting applications through the NIR optical transparency window of tissue between 650 and 950 nm. A power conversion efficiency beyond 30% and EQE over 80% were achieved under low-flux NIR illumination below 1  $\mu\text{W}/\text{mm}^2$ . The  $(\text{NH}_4)_2\text{S}$  and PECVD  $\text{Si}_3\text{N}_4$  passivation methods improved the device performance dramatically by reducing the surface/sidewall recombination losses. The optimized device structure was free of performance degradation from shunt leakage under low-flux illumination. High-efficiency GaAs PV cell under NIR low-flux illumination makes wireless PV energy harvesting through a biological tissue into a feasible approach, where further improvements may be accomplished by further reduction in edge effects and optical shadowing from electrical contacts.

## REFERENCES

[1] M. C. Frost and M. E. Meyerhoff, “Implantable chemical sensors for real-time clinical monitoring: Progress and challenges,” *Current Opinion Chem. Biol.*, vol. 6, no. 5, pp. 633–641, 2002.

[2] R. K. Meruva and M. E. Meyerhoff, “Catheter-type sensor for potentiometric monitoring of oxygen, pH and carbon dioxide,” *Biosensors Bioelectron.*, vol. 13, no. 2, pp. 201–212, 1998.

[3] D. S. Bindra *et al.*, “Design and *in vitro* studies of a needle-type glucose sensor for subcutaneous monitoring,” *Anal. Chem.*, vol. 63, no. 17, pp. 1692–1696, 1991.

[4] L. Y. Chen *et al.*, “Continuous wireless pressure monitoring and mapping with ultra-small passive sensors for health monitoring and critical care,” *Nature Commun.*, vol. 5, p. 5028, Oct. 2014.

[5] S.-K. Kang *et al.*, “Bioresorbable silicon electronic sensors for the brain,” *Nature*, vol. 530, no. 7588, pp. 71–76, 2016.

[6] A. Cadei, A. Dionisi, E. Sardini, and M. Serpelloni, “Kinetic and thermal energy harvesters for implantable medical devices and biomedical autonomous sensors,” *Meas. Sci. Technol.*, vol. 25, no. 1, p. 012003, 2013.

[7] M. A. Hannan, S. Mutashar, S. A. Samad, and A. Hussain, “Energy harvesting for the implantable biomedical devices: Issues and challenges,” *Biomed. Eng. Online*, vol. 13, no. 1, p. 79, 2014.

[8] N. S. Hudak and G. G. Amatucci, “Small-scale energy harvesting through thermoelectric, vibration, and radiofrequency power conversion,” *J. Appl. Phys.*, vol. 103, no. 10, p. 5, 2008.

[9] R.-F. Xue, K.-W. Cheng, and M. Je, “High-efficiency wireless power transfer for biomedical implants by optimal resonant load transformation,” *IEEE Trans. Circuits Syst. I, Reg. Papers*, vol. 60, no. 4, pp. 867–874, Apr. 2013.

[10] J.-D. Kim, C. Sun, and I.-S. Suh, “A proposal on wireless power transfer for medical implantable applications based on reviews,” in *Proc. IEEE Wireless Power Transf. Conf. (WPTC)*, May 2014, pp. 166–169.

[11] A. M. Smith, M. C. Mancini, and S. Nie, “Bioimaging: Second window for *in vivo* imaging,” *Nature Nanotechnol.*, vol. 4, no. 11, pp. 710–711, 2009.

[12] R. Weissleder, “A clearer vision for *in vivo* imaging,” *Nature Biotechnol.*, vol. 19, no. 4, p. 316, 2001.

[13] B. M. Kayes *et al.*, “27.6% conversion efficiency, a new record for single-junction solar cells under 1 sun illumination,” in *Proc. 37th IEEE Photovolt. Spec. Conf. (PVSC)*, Jun. 2011, pp. 000004–000008.

[14] A. S. Teran *et al.*, “Energy harvesting for GaAs photovoltaics under low-flux indoor lighting conditions,” *IEEE Trans. Electron Devices*, vol. 63, no. 7, pp. 2820–2825, Jul. 2016.

[15] A. S. Teran *et al.*, “AlGaAs photovoltaics for indoor energy harvesting in mm-scale wireless sensor nodes,” *IEEE Trans. Electron Devices*, vol. 62, no. 7, pp. 2170–2175, Jul. 2015.

[16] N. H. Reich *et al.*, “Crystalline silicon cell performance at low light intensities,” *Solar Energy Mater. Solar Cells*, vol. 93, no. 9, pp. 1471–1481, 2009.

[17] E. Moon, D. Blaauw, and J. D. Phillips, “Small-area Si photovoltaics for low-flux infrared energy harvesting,” *IEEE Trans. Electron Devices*, vol. 64, no. 1, pp. 15–20, Jan. 2017.

[18] T. B. Stellwag *et al.*, “Effects of perimeter recombination on GaAs-based solar cells,” in *Proc. Conf. Rec. 21st IEEE Photovolt. Spec.*, May 1990, pp. 442–447.

[19] A. Haeblerlin *et al.*, “The first batteryless, solar-powered cardiac pacemaker,” *Heart Rhythm*, vol. 12, no. 6, pp. 1317–1323, 2015.

[20] K. Song *et al.*, “Subdermal flexible solar cell arrays for powering medical electronic implants,” *Adv. Healthcare Mater.*, vol. 5, no. 13, pp. 1572–1580, 2016.

[21] K. Murakawa, M. Kobayashi, O. Nakamura, and S. Kawata, “A wireless near-infrared energy system for medical implants,” *IEEE Eng. Med. Biol. Mag.*, vol. 18, no. 6, pp. 70–72, Nov. 1999.

[22] K. Goto, T. Nakagawa, O. Nakamura, and S. Kawata, “An implantable power supply with an optically rechargeable lithium battery,” *IEEE Trans. Biomed. Eng.*, vol. 48, no. 7, pp. 830–833, Jul. 2001.

[23] E. Moon, D. Blaauw, and J. D. Phillips, “Subcutaneous photovoltaic infrared energy harvesting for bio-implantable devices,” *IEEE Trans. Electron Devices*, vol. 64, no. 5, pp. 2432–2437, May 2017.

[24] *Sentaurus Device User Guide Version*, Synopsys, Mountain View, CA, USA, 2013.

[25] R. W. Miles, K. M. Hynes, and I. Forbes, “Photovoltaic solar cells: An overview of state-of-the-art cell development and environmental issues,” *Progr. Cryst. Growth Characterization Mater.*, vol. 51, nos. 1–3, pp. 1–42, 2005.

[26] K. Remashan and K. N. Bhat, “Combined effect of  $(\text{NH}_4)_2\text{S}_x$  treatment and post-metallization annealing with plasma-enhanced chemical vapour deposition silicon nitride gate dielectric on the GaAs metal-insulator-semiconductor characteristics and the photoluminescence characteristics of GaAs substrates,” *Semicond. Sci. Technol.*, vol. 17, no. 3, p. 243, 2002.

- [27] H. Oigawa, J.-F. Fan, Y. Nannichi, H. Sugahara, and M. Oshima, "Universal passivation effect of  $(\text{NH}_4)_2\text{S}_x$  treatment on the surface of III-V compound semiconductors," *Jpn. J. Appl. Phys.*, vol. 30, no. 3A, p. L322, 1991.
- [28] M. S. Carpenter, M. R. Melloch, M. S. Lundstrom, and S. P. Tobin, "Effects of  $\text{Na}_2\text{S}$  and  $(\text{NH}_4)_2\text{S}$  edge passivation treatments on the dark current-voltage characteristics of GaAs *pn* diodes," *Appl. Phys. Lett.*, vol. 52, no. 25, pp. 2157–2159, 1988.
- [29] Y. Xuan, H.-C. Lin, and D. Y. Peide, "Simplified surface preparation for GaAs passivation using atomic layer-deposited high- $\kappa$  dielectrics," *IEEE Trans. Electron Devices*, vol. 54, no. 8, pp. 1811–1817, Aug. 2007.
- [30] C. Riordan and R. Hulstron, "What is an air mass 1.5 spectrum? (Solar cell performance calculations)," in *Proc. Conf. Rec. 21st IEEE Photovolt. Spec.*, May 1990, pp. 1085–1088.
- [31] K. Remashan and K. N. Bhat, "Silicon nitride/ $(\text{NH}_4)_2\text{S}_x$  passivation of n-GaAs to unpin the Fermi level," *Electron. Lett.*, vol. 32, no. 7, pp. 694–695, Mar. 1996.
- [32] Y. Lee *et al.*, "A modular 1 mm<sup>3</sup> die-stacked sensing platform with low power I<sup>2</sup>C inter-die communication and multi-modal energy harvesting," *IEEE J. Solid-State Circuits*, vol. 48, no. 1, pp. 229–243, Jan. 2013.
- [33] M. T. Sheldon, C. N. Eisler, and H. A. Atwater, "GaAs passivation with trioctylphosphine sulfide for enhanced solar cell efficiency and durability," *Adv. Energy Mater.*, vol. 2, no. 3, pp. 339–344, 2012.
- [34] C. N. Eisler, M. T. Sheldon, and H. A. Atwater, "Enhanced performance of small GaAs solar cells via edge and surface passivation with trioctylphosphine sulfide," in *Proc. 38th IEEE Photovolt. Spec. Conf. (PVSC)*, Jun. 2012, pp. 000937–000940.
- [35] T. B. Stellwag, M. R. Melloch, M. S. Lundstrom, M. S. Carpenter, and R. F. Pierret, "Orientation-dependent perimeter recombination in GaAs diodes," *Appl. Phys. Lett.*, vol. 56, no. 17, pp. 1658–1660, 1990.
- [36] C. H. Henry, R. A. Logan, and F. R. Merritt, "The effect of surface recombination on current in  $\text{Al}_x\text{Ga}_{1-x}\text{As}$  heterojunctions," *J. Appl. Phys.*, vol. 49, no. 6, pp. 3530–3542, 1978.
- [37] IXYS Corporation. (2010). *KXOB22-12X1*. [Online]. Available: <https://docs.google.com/viewerng/viewer?url=http://ixapps.ixys.com/DataSheet/KXOB22-12X1L-DATA-SHEET-20130902.pdf>
- [38] W. Shockley and H. J. Queisser, "Detailed balance limit of efficiency of *p-n* junction solar cells," *J. Appl. Phys.*, vol. 32, no. 3, pp. 510–519, 1961.
- [39] G. Mariani, A. C. Scofield, C.-H. Hung, and D. L. Huffaker, "GaAs nanopillar-array solar cells employing *in situ* surface passivation," *Nature Commun.*, vol. 4, p. 1497, Feb. 2013.
- [40] C.-C. Chang *et al.*, "Electrical and optical characterization of surface passivation in GaAs nanowires," *Nano Lett.*, vol. 12, no. 9, pp. 4484–4489, 2012.
- [41] G. Mariani, P.-S. Wong, A. M. Katzenmeyer, F. Léonard, J. Shapiro, and D. L. Huffaker, "Patterned radial GaAs nanopillar solar cells," *Nano Lett.*, vol. 11, no. 6, pp. 2490–2494, 2011.



**Eunseong Moon** (S'16) received the B.S. degree in electrical engineering from Chung-Ang University, Seoul, South Korea, in 2012, and the M.S. degree in electrical engineering from the University of Michigan, Ann Arbor, MI, USA, in 2015, where he is currently pursuing the Ph.D. degree.

His current research interests include photovoltaic energy harvesting for millimeter-scale systems.



**David Blaauw** (SM'07–F'12) received the B.S. degree in physics and computer science from Duke University, Durham, NC, USA, in 1986, and the Ph.D. degree in computer science from the University of Illinois, Urbana–Champaign, IL, USA, in 1991.

Since 2001, he has been with the faculty at the University of Michigan, where he is currently a Professor.



**Jamie D. Phillips** (M'01–SM'06) received the B.S., M.S., and Ph.D. degrees in electrical engineering from the University of Michigan, Ann Arbor, MI, USA.

He was a Post-Doctoral Researcher with Sandia National Laboratories, Albuquerque, NM, USA, and a Research Scientist at the Rockwell Science Center. In 2002, he joined the faculty at the University of Michigan, where he is currently an Arthur F. Thurnau Professor.